Analysis and Suppression of Parasitic Processes in Noncollinear Optical Parametric Amplifiers

Introduction

Optical parametric amplifiers (OPA's) are widely used as sources of broadly tunable femtosecond pulses. Critically phase matched borate crystals, such as beta-barium borate (BBO), lithium borate (LBO), and bismuth borate (BiBO) have been employed to generate tunable ultrashort pulses from the visible to the near-infrared wavelength range.[1–3] In particular, a noncollinear OPA (NOPA) allows for ultra-broad gain bandwidth that supports few-cycle pulse durations.[4,5] Signal gain of 10^3 to 10^6 can be achieved within millimeter-long crystals as a result of perfect phase matching and large nonlinear coefficients. The lack of energy storage and low residual absorption in the crystals makes it possible to scale OPA's to several watts of average output power at pulse energies ranging from the sub-μJ level to >100 μJ (Refs. 6–8). Large-aperture crystals of deuterated potassium dihydrogen phosphate (DKDP) create the potential for ultra-intense optical parametric chirped-pulse–amplification (OPCPA) systems (>10^{23} W/cm^2) using kilojoule Nd:glass lasers as pump sources.[9,10]

Parasitic nonlinear processes can significantly degrade the performance of OPA's.[2,11] For example, frequency doubling of one or more of the interacting waves can lead to spectral deformation and reduced efficiency. This article presents a detailed study of parasitic second-harmonic generation of signal and idler waves. The analysis focuses on critically phase matched NOPA's, but similar issues can occur in quasi-phase-matched materials.[12] Experimental observations are presented for two BBO-based NOPA systems. The first system is a MHz-rate NOPA that is seeded by white-light continuum generated in sapphire—a common choice for ultrafast time-dependent spectroscopy.[13] The second system has been optimized for amplification of an ultra-broadband width ranging from 650 to 1050 nm to support few-cycle pulse durations. The experimental observations agree well with the results of a 2-D numerical model that was used to evaluate the influence of parasitic processes on the NOPA's overall efficiency.

To avoid unwanted parasitic processes, different crystals and noncollinear phase-matching configurations can be used. For this purpose, calculations of the phase-matching properties for broadband BBO, LBO, BiBO, and DKDP NOPA's are presented. These results allow one to identify configurations that are free from phase-matched parasitic second-harmonic–generation (SHG) processes over the desired signal-wavelength range.

Noncollinear Phase-Matching Geometry

NOPA's achieve broadband gain by having a noncollinear angle α between the pump and signal to match the group velocity of the signal and idler.[3,14] Figure 126.37 shows a common configuration for BBO, a crystal widely used for visible-wavelength NOPA's. The pump is extraordinary polarized (*e* wave) and its Poynting vector (S_P) and wave vector (k_P) are separated by an angle ρ. In BBO, the optimum α for the broadest gain is comparable to ρ. For example, $\rho = 3.3°$ and $\alpha = 2.6°$ when the wavelengths of the pump and signal are chosen to $\lambda_P = 523$ nm and $\lambda_S = 800$ nm, respectively. Pump–signal birefringent walk-off is partially compensated by positioning the signal on the side to which the pump walks off, away from the crystal axis [see Fig. 126.37(b)]. In this case, the angle between the pump and signal Poynting vectors is $\rho - \alpha = 0.7°$. The idler is angularly dispersed (5×10^{-3} deg/nm) and has an average angle relative to the signal of ~7.4°.

Since the signal and idler are ordinary polarized (*o* waves), identical phase-matching conditions exist for any orientation of the signal *wave vector* around the pump wave vector, provided α is kept constant. This is shown in Fig. 126.37(a) as a circle around the pump wave vector. The largest pump–signal walk-off occurs when the angle between their Poynting vectors is $\rho + \alpha = 5.9°$ [see Fig. 126.37(c)]. The two extremes are referred to as walk-off compensating (WC) and non-walk-off compensating (NWC), respectively.

Figure 126.38 shows the signal angles θ_S at which signal wavelengths are phase matched for a BBO NOPA pumped at 523 nm. Curves for several noncollinear angles α are shown (in red) for both the (a) WC and (b) NWC configurations. The NOPA phase matching has, to first order, the broadest bandwidth when the curves are horizontal;[3,15] that is, a choice of

internal signal angle achieves perfect phase matching for the broadest range of signal wavelengths. Also shown (in blue) are the phase-matching curves for signal SHG. For the WC case, certain combinations of θ_S and α simultaneously phase match both the NOPA and signal SHG processes; therefore, parasitic SHG can occur.

Figure 126.39 shows a calculation of the phase-matching conditions for idler SHG. The internal angle of the idler wave to the crystal axis, θ_I, was calculated to compensate the pump wave's vector component k_P, perpendicular to the signal wave vector k_S. Two values of α for both the WC and NWC configurations are shown (red curves). The phase-matching curves for idler SHG are shown in blue. In the WC configuration, phase matching is achieved at an idler wavelength of 1265 nm, and the angular deviations between the idler and the SHG phase-matching curve are small, in the wavelength range between 1100 nm and 1500 nm. In contrast, the NWC configuration avoids idler SHG since the phase-matched idler wavelengths (865 nm and 900 nm) are typically not present.

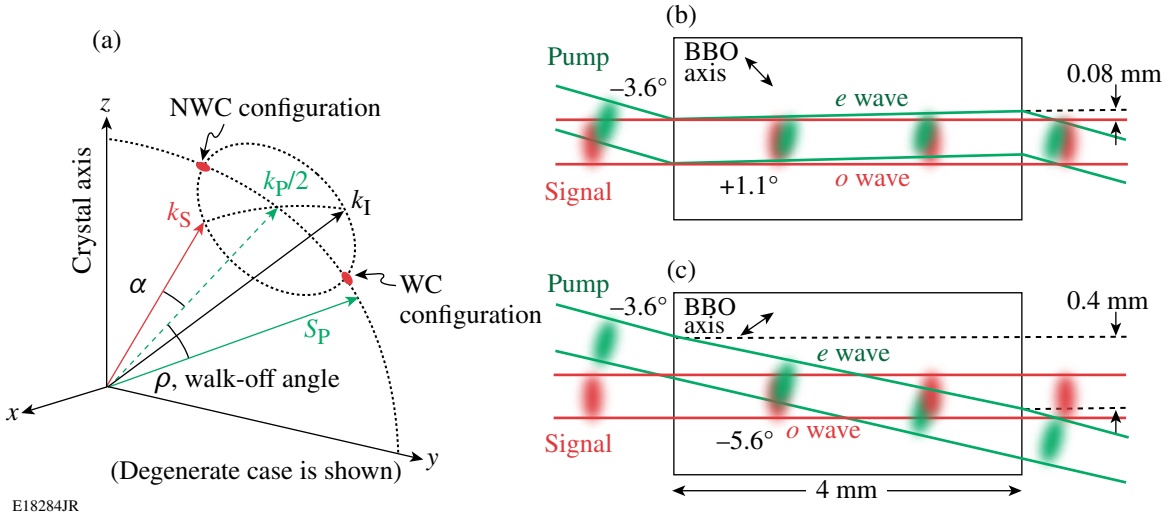

Figure 126.37
(a) Geometry for critical phase matching in a uniaxial crystal. The noncollinear angle between the pump and signal wave vectors is α. The walk-off angle between the pump Poynting vector (S_P) and signal wave vector is ρ. (b) Definition of the walk-off compensating (WC) configuration for negative uniaxial crystals. (c) Non-walk-off compensating (NWC) configuration. The idler wave vectors are angularly dispersed (not shown) and angles are exaggerated for clarity.

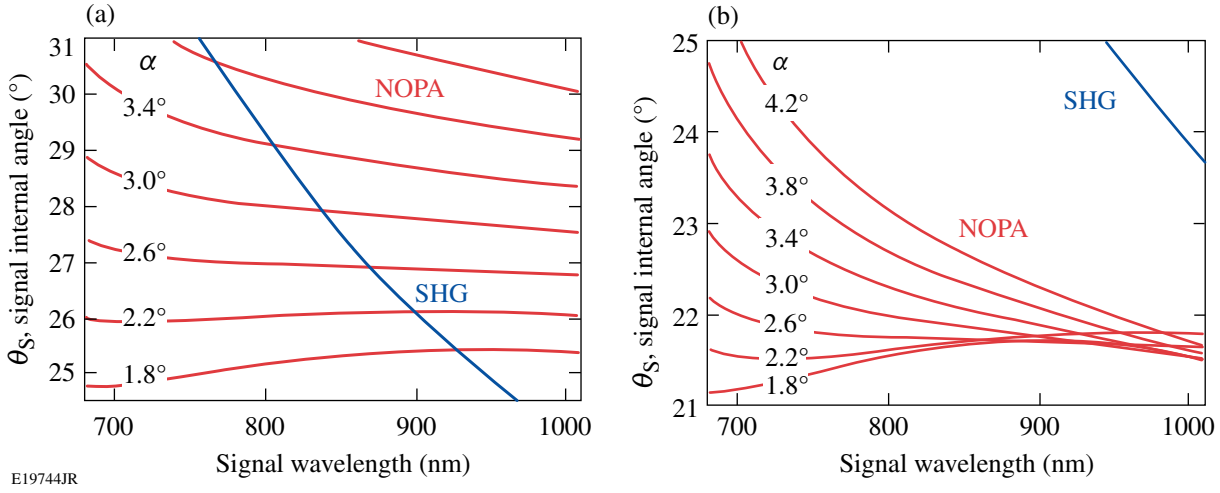

Figure 126.38
NOPA phase-matching curves (red) for BBO pumped at 523 nm for several noncollinear angles α: (a) the walk-off compensating (WC) and (b) the non-walk-off compensating (NWC) configurations. The phase-matching curves for signal SHG are shown in blue.

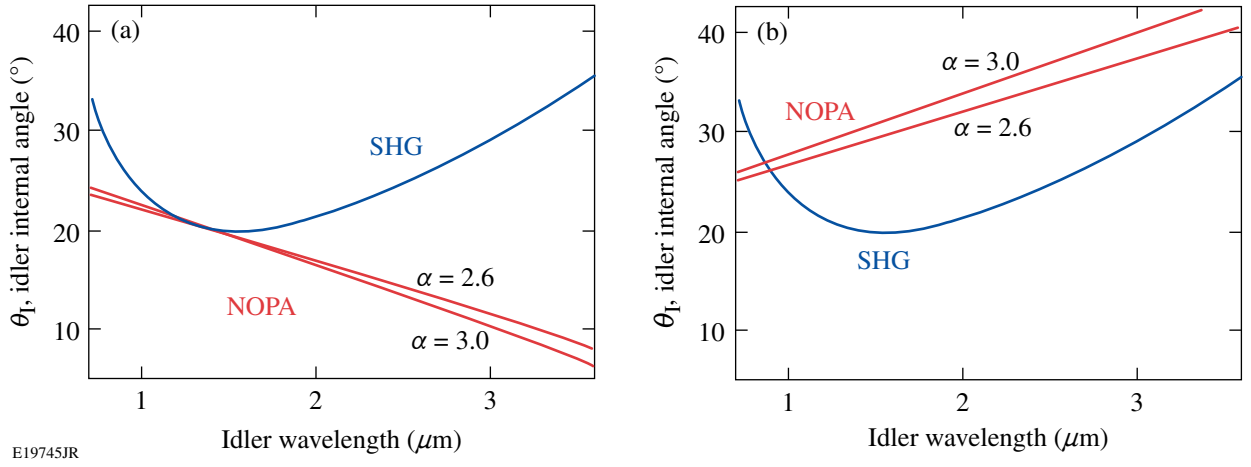

Figure 126.39
The idler wavelengths and internal angles for NOPA phase matching in BBO pumped at 523 nm for two values of α (in red): (a) the WC and (b) the NWC configurations. The phase-matching curves for idler SHG are shown in blue.

Experimental Observation of Parasitic Signal SHG

Parasitic processes were experimentally investigated using a BBO-based NOPA pumped at 1 MHz by a fiber chirped-pulse–amplifier (FCPA) system. A schematic of the system is shown in Fig. 126.40. Pulses from a mode-locked oscillator were stretched from 220 fs to 180 ps, down-selected from 38 MHz to 1 MHz, and amplified by a chain of four ytterbium-doped fiber amplifiers. A large-mode-area photonic-crystal fiber amplifier was used for the final stage, producing 12-μJ pulses centered at 1047 nm (Ref. 16). The compressor used two multilayer dielectric gratings (1740 lines/mm) to produce 9-μJ, 250-fs pulses. A portion of the energy (20%) was picked off and

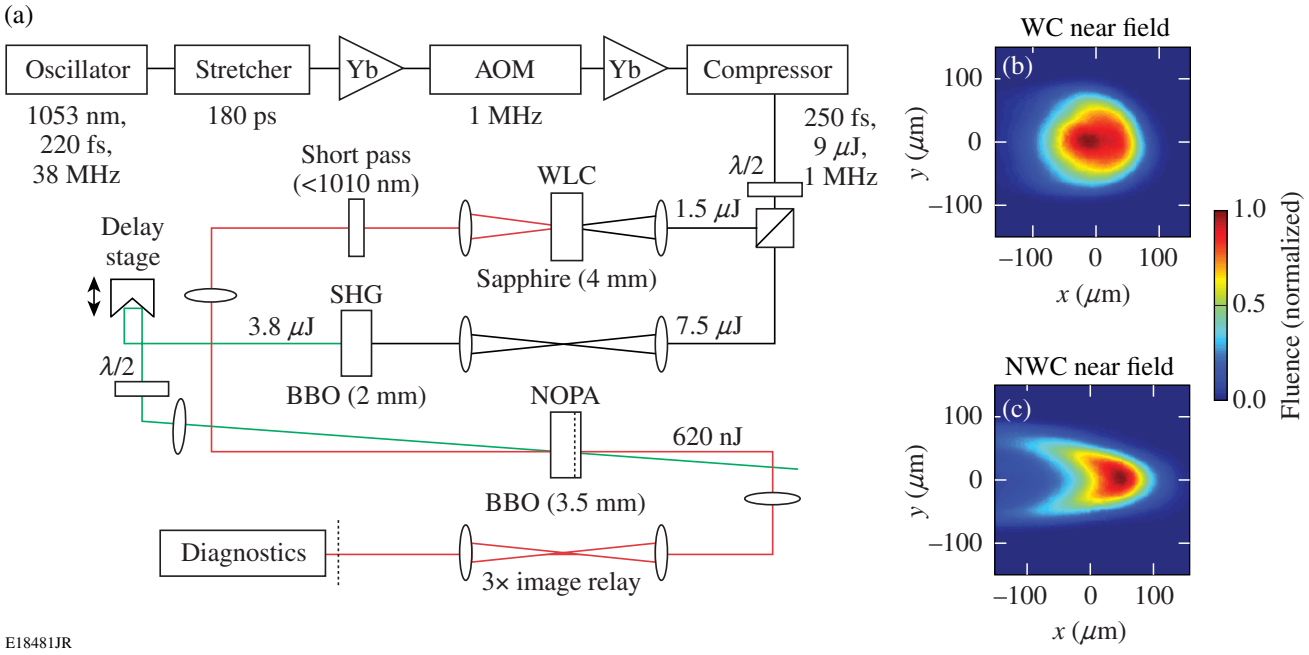

Figure 126.40
(a) Experimental setup. Yb: ytterbium-doped fiber amplifiers; AOM: acousto-optic modulator; WLC: white-light continuum; SHG: second-harmonic generation; NOPA: noncollinear optical parametric amplifier. Near-field profiles of the amplified beams for (b) walk-off compensating (WC) and (c) non-walk-off compensating (NWC) configurations.

weakly focused into a static 4-mm sapphire plate to generate a chirped white-light continuum (WLC) seed.[17] The rest was doubled in a 2-mm BBO crystal, producing 3.8-μJ pulses at 523 nm for pumping the NOPA.

The BBO crystal used in the NOPA was 4 mm long and was cut at an angle such that the seed beam was approximately perpendicular to the crystal face (27.1° and 21.6° for the WC and NWC geometries, respectively). The pump and seed were focused into the NOPA crystal with ~120-μm beam waists. The pump–signal walk-off lengths, defined as the distance required for a change in separation equal to their beam waists, were 8.2 mm for WC and 0.96 mm for NWC. The impact of pump–signal walk-off is clearly seen in the near-field beam profiles [Figs. 126.40(a) and 126.40(b)]. In the WC case, the near field is approximately Gaussian. In contrast, in the NWC case, there is a large asymmetry along the direction of walk-off (x–z plane). Despite this significant difference, the maximum signal power obtained for each configuration was roughly equal at ~850 nJ, when the seed delay and phase matching were optimized for 780 nm.

Amplified signal spectra for the two walk-off configurations are shown in Fig. 126.41. For the WC configuration, parasitic signal SHG was phase matched in the center of the gain band [Fig. 126.41(a)]. This resulted in a narrow spectral line at 412 nm (shown in blue), a large notch in the center of the signal spectrum at 824 nm, and smaller notches on either side at 788 nm and 865 nm. The side notches are due to non-degenerate sum–frequency generation: $(788\text{ nm})^{-1} + (865\text{ nm})^{-1} = (412\text{ nm})^{-1}$. No parasitic signal SHG was observed for the NWC configuration, and the signal spectrum had a smooth Gaussian-like shape [Fig. 126.41(b)].

Second-harmonic generation from the idler was also observed in the WC configuration. Figure 126.42 shows a measurement of its spectrum. Like the idler, which is angularly dispersed because of noncollinear phase matching, the idler second harmonic (SH) is angularly dispersed, producing a visible rainbow at the output of the amplifier that extends from

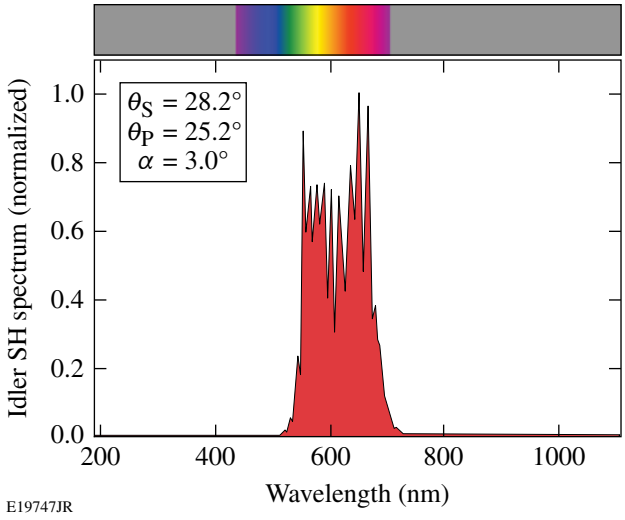

Figure 126.42
Spectra measured from idler SHG for the WC configuration. The spectrum spans much of the visible spectrum, as shown by the color bar above.

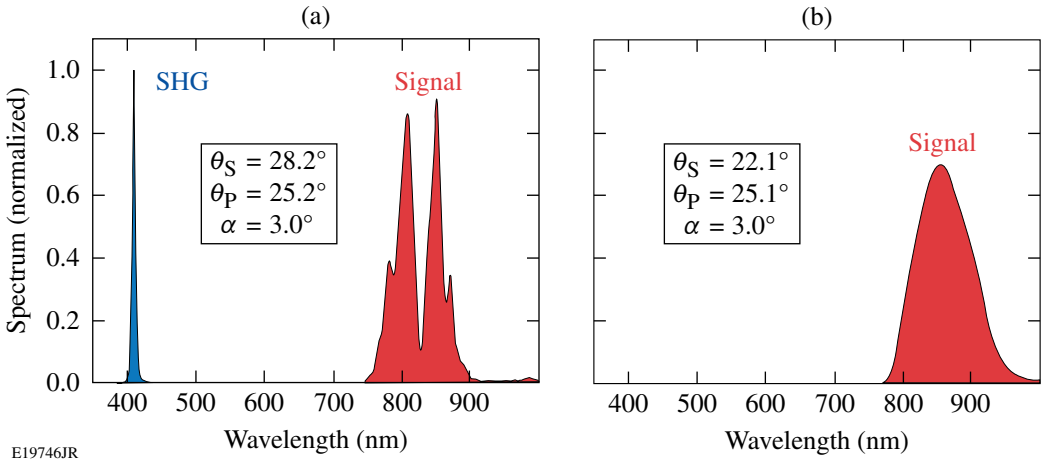

Figure 126.41
Signal spectra for (a) the WC and (b) the NWC configurations. The pump angle θ_P and noncollinear angle α were similar in both cases. In the WC configuration, the signal angle θ_S of 28.2° made it possible for parasitic second-harmonic generation to produce a narrow spectral line at 410 nm, leaving notches in the signal spectrum in the 780- to 870-nm range.

550 nm to 700 nm. This observation fits well to the phase-matching calculations shown in Fig. 126.39. A rough estimate of the idler SH energy is 0.1 to 0.4 nJ, which is less than 1% of the signal energy. Errors in this measurement result from calibration uncertainties for the broadband edge filter used to separate the idler and its second harmonic.

Numerical Model for Parasitic Signal and Idler SHG

The growth of parasitic signal and idler SHG was investigated using a 2-D numerical model. The equations of motion for the relevant optical fields were integrated using a split-step code that employed a fourth-order Runge–Kutta algorithm. The nonlinear propagation was modeled using Eqs. (1) for the field amplitudes in the time domain, $A_j(z,t)$, where j = S, I, P, SSH, and ISH for the signal, idler, pump, signal SH, and idler SH fields, respectively.

$$\frac{dA_S}{dz} = i\frac{2\omega_S d_{eff}}{n_S c}\left(A_I^* A_P - A_S^* A_{SSH}\right),$$

$$\frac{dA_I}{dz} = i\frac{2\omega_I d_{eff}}{n_I c}\left(A_S^* A_P - A_I^* A_{ISH}\right),$$

$$\frac{dA_P}{dz} = i\frac{2\omega_P d_{eff}}{n_P c}A_S A_I, \qquad (1)$$

$$\frac{dA_{SSH}}{dz} = -i\frac{2\omega_{SSH} d_{eff}}{n_{SSH} c}A_S^2,$$

$$\frac{dA_{ISH}}{dz} = -i\frac{2\omega_{ISH} d_{eff}}{n_{ISH} c}A_I^2.$$

A constant nonlinear coefficient d_{eff} was assumed to be 2.16 pm/V (Ref. 18). Linear propagation effects such as dispersion and phase matching were included in the frequency domain using conjugate field amplitudes $a_j(z,\Omega)$, calculated from the time-domain amplitude using

$$a_j(z,\Omega) = \mathrm{FFT}^{-1}\left[A_j(z,t), t \rightarrow \Omega\right]. \qquad (2)$$

Ω is defined as the optical-frequency difference relative to the field's center frequency ω_j. The linear part of the split-step propagation, for step size h, was given by

$$a_j(z+h,\Omega) = a_j(z,\Omega)e^{in_j h\left(\omega_j+\Omega\right)/c - ih\Omega/v_S}, \qquad (3)$$

where n_j is the frequency-dependent refractive index calculated using Sellmeier equations for BBO.[19] The second term in the exponent is added so that calculations are done in the frame of the signal pulse traveling with a group velocity v_S.

Figure 126.43 compares measured and simulated signal spectra for the WC configuration. Results are plotted for a range of signal angles θ_S. Similar features are seen in both, despite

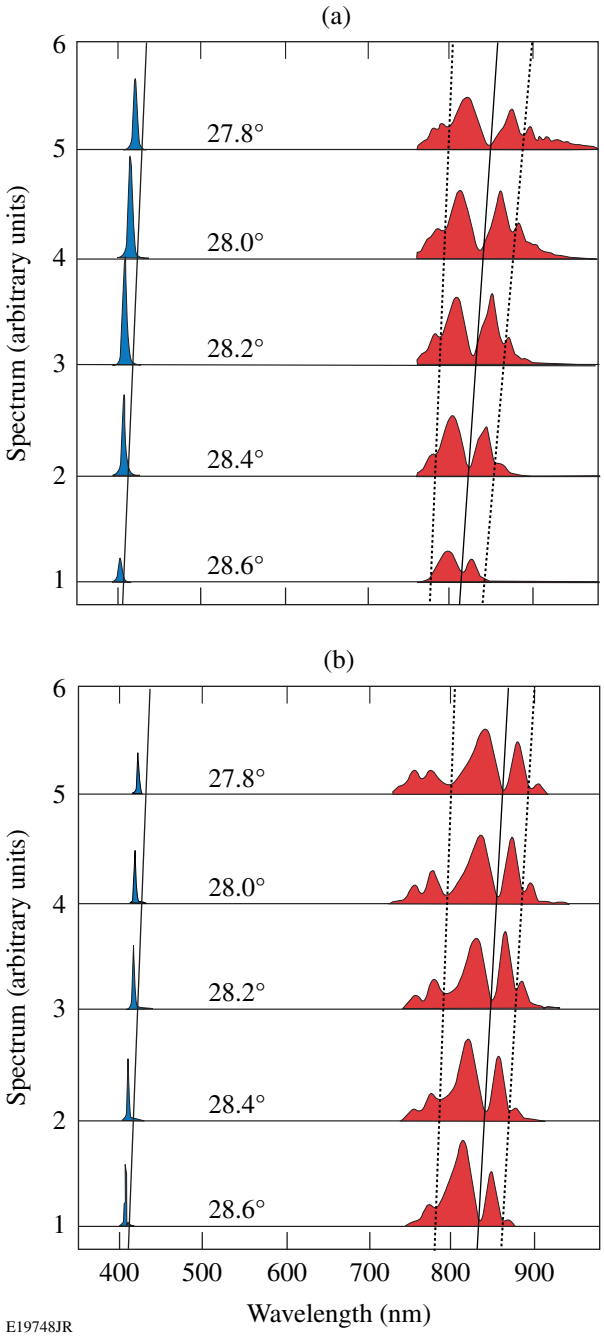

Figure 126.43
Comparison of (a) experimental measurements and (b) numerical simulations for a range of signal angles in the WC configuration.

the fact that the simulations use a simple 2-D model that does not include effects of spatial walk-off and intensity variation over the pump, signal, and idler beams. In both cases, notches are seen in the signal spectra corresponding to the generation of signal SHG, and the notches shift to longer signal wavelengths as the signal angle is reduced, consistent with the SHG phase-matching curves shown in Fig. 126.38. The calculated spectral features of parasitic signal SHG agree well with the experimental results.

Impact of Signal SHG on NOPA Efficiency

One benefit of an accurate model is the ability to evaluate the impact of parasitic processes by comparing results calculated either with or without the process. Furthermore, the axial evolution of each field within the crystal can be calculated to show the exchange of energy between the fields. The parameters shown in Table 126.VI were chosen for a case study of a BBO NOPA, corresponding approximately to the experimental configuration in Fig. 126.40.

Figure 126.44 shows amplified signal spectra for cases where the signal SHG was either included or suppressed in the model. The sharp notch and signal SH are evident in Fig. 126.44(a). Some spectral modulation is also seen in Fig. 126.44(b), even though SHG was suppressed in the simulation and the experimentally measured spectra were smooth [see Fig. 126.41(b)]. In this case the modulation is due to reconversion of the signal. The 2-D nature of the model, which considers only one value of peak temporal intensity for the pump and signal, means that averaging of reconversion effects over the Gaussian beam were not included and the spectral structure was not averaged away.

The impact of signal SHG on peak amplifier efficiency is shown in Fig. 126.45. Simulations predict that 10% of the signal pulse energy is lost to SHG at the optimum crystal length of 2.3 mm. In contrast, simulations of idler SHG show that a small *increase* in efficiency of a few percent can be expected when idler SHG is present. Similar effects have been observed in pulsed optical parametric oscillators (OPO's); absorption of

Table 126.VI: Input parameters for signal SHG case study.

Parameter	Value	Parameter	Value
Noncollinear angle (α)	3.1°	Signal spectral phase (ϕ_2)	200 fs^2
Signal angle (θ_S)	28.2°	Pump width (Gaussian) (τ)	250 fs
Pump angle (θ_P)	25.1°	Pump–signal delay at input	75 fs
Signal center wavelength (λ_S)	820 mm	Beam widths ($1/e^2$)	120 μm
Pump wavelength (λ_P)	523.5 nm	Signal input energy (E_S)	0.1 nJ
Input signal bandwidth ($\Delta\lambda_S$)	250 nm	Pump input energy (E_P)	2 μJ
Order of Gaussian signal spectrum	Tenth order	BBO crystal length (l_C)	3 mm

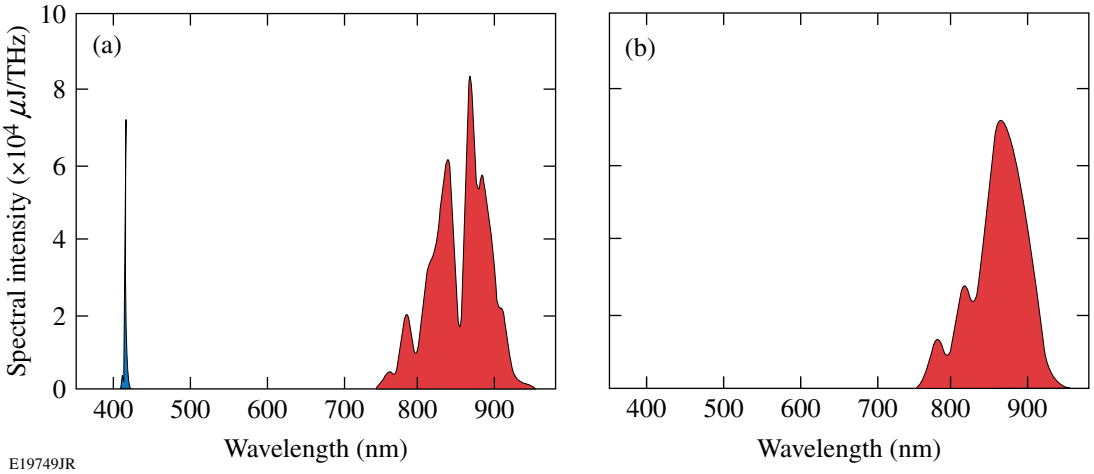

Figure 126.44
Spectra for simulation case study. Signal SHG (a) turned on and (b) turned off in the model.

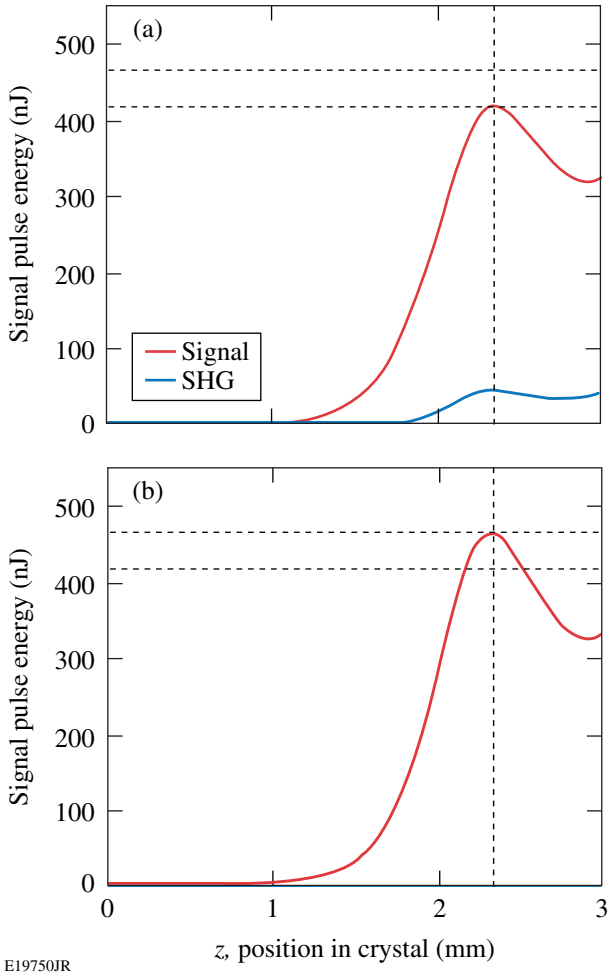

Figure 126.45
Simulated signal energy along the crystal, (a) with and (b) without signal SHG. In both cases signal reconversion means that the length for optimum efficiency is 2.3 mm. When SHG is included in the simulations, 10% of the signal energy at this length is lost to the parasitic process.

the idler removes it from the three-wave interaction, increasing the threshold at which the signal is reconverted to the pump.[20]

Parasitic Processes in Few-Cycle NOPA

NOPA's can support the extremely large optical bandwidth required by few-cycle pulses. Parasitic nonlinearities may occur over a significant wavelength range of the signal and idler. To investigate parasitic SHG effects over a larger spectral bandwidth, measurements with a few-cycle NOPA were performed. The experimental setup of the system is shown in Fig. 126.46 and is similar to the one presented in Refs. 5 and 7. A Ti:sapphire oscillator (Femtolasers Rainbow) delivering few-cycle pulses is used for seeding both the NOPA and a state-of-the-art FCPA system. The FCPA system delivers 900-μJ, 650-fs pump pulses that are frequency doubled in a 1-mm BBO crystal with an efficiency of 56%, resulting in 500-μJ pump pulses for the NOPA. Focusing to 100 GW/cm^2 provides a gain of 5×10^4. The signal pulses traverse a pulse-shaping device and a prism stretcher before being imaged into the BBO crystal. The noncollinear angle is 2.5° to achieve broadband phase matching. This is slightly lower than the angle for group-velocity matching of signal and idler (2.6°). As a result, the phase matching is improved in the spectral wings, while a slight phase mismatch is generated in the center. This configuration leads to a larger effective gain bandwidth, therefore shorter pulses at the output of the system.[15] Because of the high pump intensity, the 0.5-nJ oscillator pulses can be amplified to 25 μJ in a single stage in both the WC and NWC configurations.

Quantitative measurements of the parasitic process were made using a bandpass filter (Newport BG.40) to separate the signal's fundamental and SH pulses. Their spectra for the WC and NWC configurations are shown in Figs. 126.47(a) and 126.47(b), respectively. The SH energy for the WC geometry measured after the filter is 1.1 μJ, corresponding to ~4% of the energy of the amplified signal. The measured spectra clearly show phase-matched SHG of 860-nm signal to 430 nm. This agrees with the phase-matching calculations for the NOPA configuration. The amplified signal spectrum shows modulation that may originate

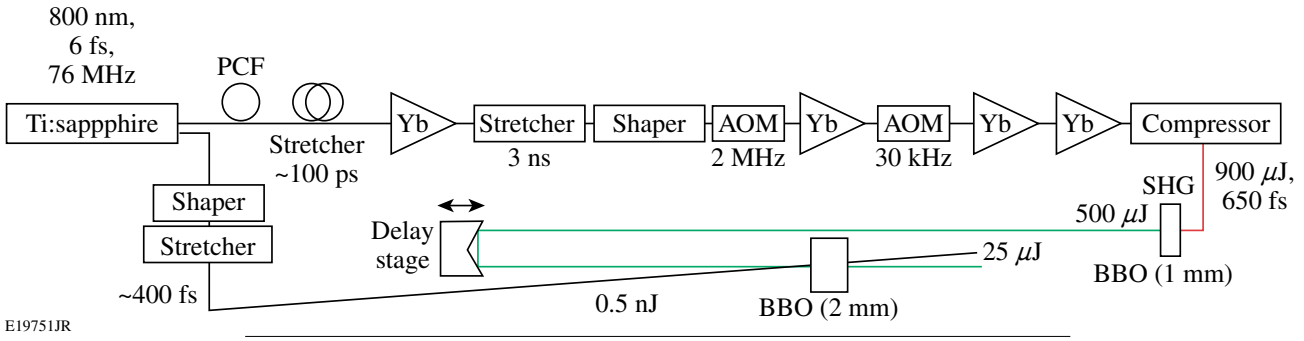

Figure 126.46
A noncollinear OPCPA setup pumped by the second harmonic of a high-energy FCPA system.

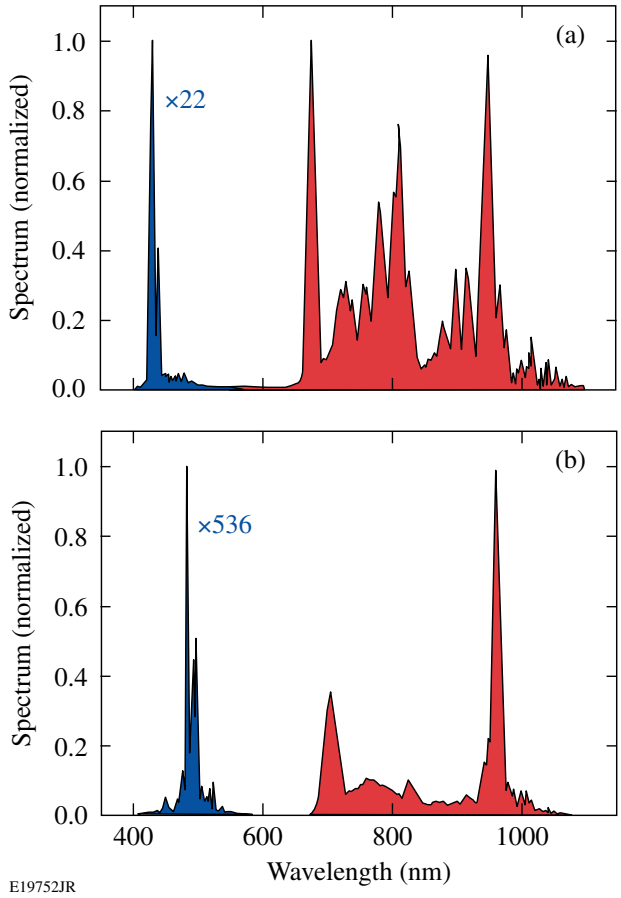

Figure 126.47
Measured spectra for (a) the WC and (b) the NWC configurations containing the signal and its second harmonic. Note that both the fundamental and the second-harmonic spectra have been normalized to their peak value, independently.

not only from signal SHG, but also from sum–frequency generation (similar to the side notches shown in Fig. 126.41).

In contrast, the parasitic signal SHG is significantly reduced in the NWC configuration and the spectrum of the amplified signal has less modulation. For the same amplified pulse energy, the signal SH power after the BG.40 filter is only 37 nJ, corresponding to ~0.1% of the amplified signal energy. Phase-matching calculations show that no signal wavelengths are perfectly phase matched in this configuration, resulting in inefficient signal SHG.

The idler SHG was also observed in the WC configuration and spanned from 550 nm to 750 nm. This is supported by the calculation of the phase-matching conditions shown in Fig. 126.39. As expected, no idler SHG was measured in the NWC configuration.

Parasitic Phase-Matching Curves for Other Common Nonlinear Crystals

Parasitic SHG processes are not limited to BBO-based NOPA's. The phase-matching curves for signal and idler SHG are shown in Fig. 126.48 for other common nonlinear crystals: LBO, BiBO, and DKDP. In all cases, the noncollinear angle was chosen for group-velocity matching of the signal and idler. The resulting signal angle within the crystal is plotted in dashed lines for both configurations, together with the corresponding SHG phase-matching curves, in Figs. 126.48(a), 126.48(c), and 126.48(e), respectively. The internal idler angles for idler SHG are plotted in Figs. 126.48(b), 126.48(d), and 126.48(f) (dashed lines). The SHG phase-matched signal and idler wavelengths for each crystal type and configuration are given in Table 126.VII.

The resulting idler wavelengths, which are phase matched for second-harmonic generation, and the corresponding signal wavelengths are displayed in Table 126.VII. The last row of Table 126.VII represents the usable parasitic SHG-free signal wavelength range around an 800-nm central wavelength. It has to be taken into account for the design of a broadband OPCPA system. In summary, the NWC configuration offers the largest parasitic-SHG-free bandwidth for all considered crystals. Furthermore, BBO in the NWC configuration seems

Table 126.VII: SHG phase-matched signal and idler wavelengths for BBO, LBO, BiBO, and DKDP in both WC and NWC configurations for NOPA's pumped by the second harmonic of Yb-based systems (λ_P = 510 to 525 nm). The corresponding signal wavelength for parasitic idler SHG is calculated from the energy conversion. The parasitic SHG free-wavelength range is summarized in the last row.

Crystal material	BBO		LBO		BiBO		DKDP	
Configuration	WC	NWC	WC	NWC	WC	NWC	WC	NWC
Signal SHG wavelength (nm)	860	1119	963	1012	889	1025	942	1090
Idler SHG wavelength (nm)	1265	864	1031/1067	983/1794	1102/2338	969	1110	951
Signal λ for idler SHG (nm)	869	1275	1029/758	1082/722	966/660	1099	961	1123
Parasitic SHG free λ range (nm)	<860	<1119	758...963	722...1012	660...889	<1025	<942	<1090

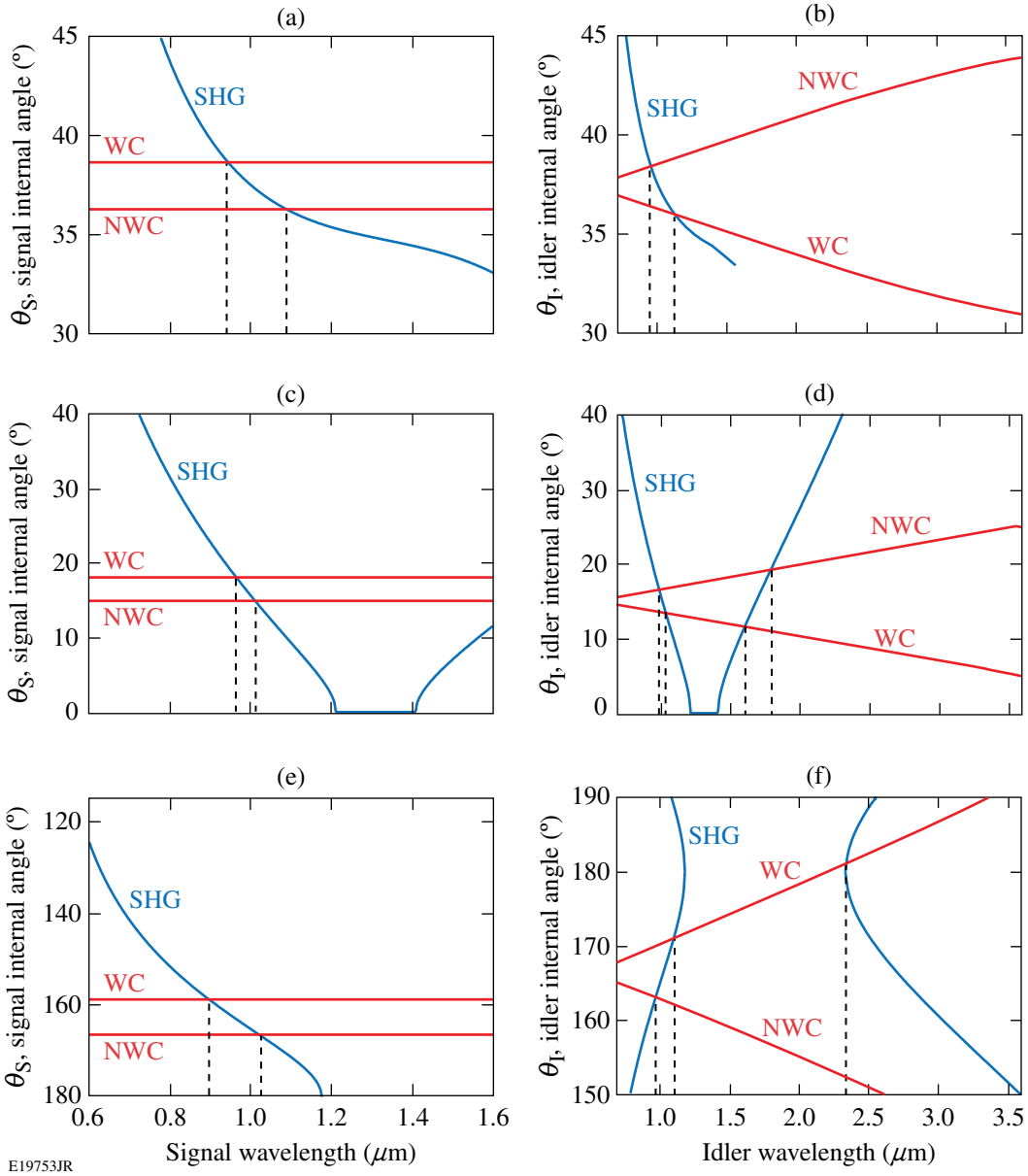

Figure 126.48
Phase-matching curves for signal (left column) and idler (right column) SHG for other common NOPA crystals: [(a),(b)] DKDP; [(c),(d)] LBO; and [(e),(f)] BiBO.

to be most suitable for ultra-broadband NOPA's since it is free of parasitic-SHG phase matching until 1129 nm. Deviations from the assumed noncollinear angles and pump wavelength will shift the SHG phase-matched wavelength slightly, although the general behavior remains the same.

Conclusions

A detailed analysis of parasitic nonlinear effects, namely second-harmonic generation of the signal and idler waves, on broadband high-repetition-rate NOPA's has been presented. Results from an experimental study of a white-light–seeded NOPA agree well with 2-D numerical simulations. Modeling shows that second-harmonic generation of the signal can reduce the NOPA output energy by 10%.

A quantitative analysis was carried out for an ultra-broadband, few-cycle NOPA. For the WC configuration, a few percent of the output is converted into signal SH, while the

effect is reduced by at least an order of magnitude for the NWC configuration. Strong spectral modulation is observed in the WC configuration that originates from SHG and SFG of the spectral components of the signal and idler. Such modulation can significantly reduce the pulse quality of the output pulses and can be avoided by using the NWC configuration. A detailed phase-matching analysis for the most common nonlinear crystals is presented as a guide for designing NOPA systems.

The NOPA application dictates which configuration is best suited. For a laser front end, for example, a symmetric near-field profile and good spectral uniformity across the beam are required. In the case of low pump-pulse energy (<10 μJ) and peak power (~10 MW), the WC geometry is the best choice, provided parasitic SHG can be avoided over the amplifier's wavelength range. For spectroscopic applications, where the bandwidth and tuning range of the signal are primary requirements, the NWC configuration is a better choice, provided that lower gain is acceptable or that the poor beam symmetry and spectral nonuniformity across the beam are tolerable. In the case of an ultra-broadband, few-cycle NOPA, the NWC configuration must be used to avoid power loss and spectral modulation on the ultra-broad spectrum. Distortions in the amplified beam can be avoided in this case by weakly focusing the high-peak-power pump laser.

ACKNOWLEDGMENT

This work has been supported by the U.S. Department of Energy Office of Inertial Confinement Fusion under Cooperative Agreement No. DE-FC52-08NA28302, the University of Rochester, and the New York State Energy Research and Development Authority. The support of DOE does not constitute an endorsement by DOE of the views expressed in this article.

This work was also supported by the German Federal Ministry of Education and Research (BMBF) with project 03ZIK455 "onCOOPtics," the Helmholtz Institute Jena, and the European Research Council under the European Union's Seventh Framework Programme (FP7/2007-2013)/ERC Grant agreement 240460. S. H. acknowledges financial support by the Carl Zeiss Stiftung Germany.

REFERENCES

1. C. Schriever *et al*., Opt. Lett. **33**, 192 (2008).
2. J. Piel *et al*., Opt. Lett. **31**, 1289 (2006).
3. G. Cerullo and S. De Silvestri, Rev. Sci. Instrum. **74**, 1 (2003).
4. A. Steinmann *et al*., Opt. Express **14**, 10,627 (2006).
5. S. Hädrich *et al*., Opt. Lett. **36**, 313 (2011).
6. J. Rothhardt *et al*., Opt. Express **15**, 16,729 (2007).
7. J. Rothhardt *et al*., Opt. Express **16**, 8981 (2008).
8. J. Rothhardt *et al*., Opt. Express **18**, 12,719 (2010).
9. Y. Tang *et al*., Opt. Lett. **33**, 2386 (2008).
10. V. V. Lozhkarev *et al*., Opt. Express **14**, 446 (2006).
11. G. Arisholm *et al*., Opt. Express **12**, 518 (2004).
12. J. Hellström *et al*., Opt. Lett. **26**, 352 (2001).
13. E. Riedle *et al*., Appl. Phys. B **71**, 457 (2000).
14. G. M. Gale *et al*., Opt. Lett. **20**, 1562 (1995).
15. D. N. Schimpf *et al*., J. Opt. Soc. Am. B **24**, 2837 (2007).
16. For more system details, see J. Bromage, J. M. Fini, C. Dorrer, and J. D. Zuegel, Appl. Opt. **50**, 2001 (2011).
17. R. R. Alfano, *The Supercontinuum Laser Source: Fundamentals with Updated References*, 2nd ed. (Springer, New York, 2006).
18. G. G. Gurzadian, V. G. Dmitriev, and D. N. Nikogosian, *Handbook of Nonlinear Optical Crystals*, 3rd rev. ed., Springer Series in Optical Sciences, Vol. 64 (Springer-Verlag, Berlin, 1999).
19. D. Eimerl *et al*., J. Appl. Phys. **62**, 1968 (1987).
20. G. Rustad, O. Farsund, and G. Arisholm, presented at Advances in Optical Materials (AIOM), Istanbul, Turkey, 16–18 February 2011 (Paper AWA25).